ACS Catalysis

Research Article

pubs.acs.org/acscatalysis

Multielement Activity Mapping and Potential Mapping in Solid Oxide Electrochemical Cells through the use of *operando* XPS

Chunjuan Zhang,[†,⊥] Michael E. Grass,[‡,⊥] Yi Yu,[†] Karen J. Gaskell,[†] Steven C. DeCaluwe,[§] Rui Chang,[‡] Gregory S. Jackson,*[,§] Zahid Hussain,[‡] Hendrik Bluhm,[∥] Bryan W. Eichhorn,*[,†] and Zhi Liu*[,‡]

[†]Department of Chemistry and Biochemistry and [§]Department of Mechanical Engineering, University of Maryland, College Park, Maryland 20742, United States

[‡]Advanced Light Source and [∥]Chemical Sciences Division, Lawrence Berkeley National Laboratory, Berkeley, California 94720, United States

Supporting Information

ABSTRACT: Spatially resolved ambient pressure X-ray photoelectron spectroscopy has been used to measure and visualize regions of electrochemical activity, local surface potential losses, overpotentials, and oxidation state changes on single sided ceria/yttria-stabilized zirconia (YSZ)/Pt solid oxide electrochemical cells. When hydrogen electro-oxidation (negative applied bias) or water electrolysis (positive applied bias) is promoted on the ceria electrocatalyst, the Ce^{3+}/Ce^{4+} ratios shift away from equilibrium values and thereby demarcate electrochemically active regions on the ceria electrode. In addition to the ceria oxidation state shifts, inactive surface impurities with high photoelectron cross sections, such as Si, can provide local markers of activity through chemical and surface potential mappings under various electrochemical conditions. Localized removal of chemically active carbonaceous surface impurities also reveals regions of electrochemical oxidation activity on the ceria electrode. Finally, we show that electrochemical polarization of solid oxide electrochemical cells under different gas environments is used to control the ceria surface chemical state and oxygen vacancy density.

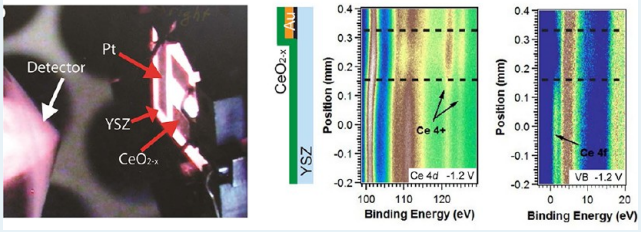

KEYWORDS: *ambient pressure XPS, ceria, solid oxide electrochemical cell, operando*

INTRODUCTION

Solid oxide electrochemical cells (SOCs) are a general class of solid-state electrochemical devices that encompass solid oxide electrolysis cells (SOECs) for fuel generation from electricity and solid oxide fuel cells (SOFCs) that convert fuels and oxygen to electric power. Although these devices have already had limited commercial success, there are still many issues that must be resolved before they become significant contributors to the alternative energy infrastructure. The lack of direct knowledge regarding the surface chemistry and electrochemical processes that govern these systems impedes the advancement of designs for membrane electrode assemblies in SOCs. The gaseous reactant environment, high operating temperatures (>600 °C) and far-from-equilibrium conditions associated with the operating devices precludes the use of most surface science analytical tools such as atomic force microscopy (AFM), scanning tunneling microscope (STM), and traditional ultra-high vacuum (UHV) X-ray photoelectron spectroscopy (XPS).

New in situ and operando methods are being developed to address these issues and are beginning to provide fundamental insight into SOC processes. These studies include in situ Raman,[1−3] near ambient-pressure X-ray photoelectron spectroscopy (AP-XPS),[4,5] X-ray diffraction (XRD),[6] X-ray absorption spectroscopy (XAS),[7] thermal imaging and vibrational spectroscopy.[8] We demonstrated the use of AP-XPS[9] to spatially resolve local surface potentials, electrochemically active regions, and shifts in surface oxidation states in operating SOCs.[4,5,10,11] Our SOCs utilize CeO_{2-x} (ceria) working electrodes (WE) with 8 mol % yttria-stabilized zirconia (YSZ) electrolyte supports and Pt counter electrodes (CE) to promote water electrolysis or hydrogen electro-oxidation depending on the applied bias. Under low effective O_2 partial pressures ($P_{O2,eff} < 10^{-15}$ bar), ceria becomes a mixed-ionic-electronic-conducting (MIEC) material that conducts oxide ions through oxide vacancies and electrons by way of a "polaron-hoping" mechanism.[12,13] Because of the MIEC behavior of ceria at low $P_{O2,eff}$ characteristic of fuel-side electrodes, electrochemically active regions can be extended beyond the three-phase boundaries (TPB) that limit other cermet electrodes where oxide-ion conductivity and electron conductivity occur in separate materials.[14]

Ceria has useful surface and bulk properties that have led to a variety of industrial applications including catalysis, electro-

Special Issue: Operando and In Situ Studies of Catalysis

Received: July 2, 2012
Revised: August 16, 2012
Published: September 21, 2012

   dx.doi.org/10.1021/cs3004243 | ACS Catal. 2012, 2, 2297−2304

chemical cell, and solar energy devices. Many of the catalytic properties of ceria can be attributed to its ability to change oxidation states over a wide temperature range at low $P_{O2,eff}$.[10,12,13] On its surface, oxygen vacancies can be rapidly formed and reoxidized, giving ceria an enhanced ability to release and store oxygen and to split H_2O in catalytic and electrocatalytic reactors. Therefore, the abilities to monitor, modify, and eventually control the ceria surface vacancy at a given pressure, temperature, and gas environment are important and highly desirable for catalysis and other related fields.

In this paper, we demonstrate high resolution mapping of local surface potentials and overpotentials in an operating SOC through the use of AP-XPS. We also employ trace foreign elements, such as Si, as convenient markers of local potential across the entire SOC surface, and volatile elements, such as carbon, are irreversibly oxidized on the ceria surface at positive bias to demarcate regions of electrochemical activity. Finally, we show that the surface Ce^{3+}/Ce^{4+} ratios, that is, surface oxygen vacancy density, can be readily modified using different bias voltages and gas environments; and such ratios are directly correlated to the filling of the ceria 4f valence state. Thus it is entirely possible to adjust the surface vacancy of ceria through electrochemical means.

EXPERIMENTAL SECTION

We purchased 8 mol % yttria-stabilized zirconia (YSZ) powder from Tosoh Inc. The powder was pressed in a coaxial stainless steel die-press. As-pressed YSZ pellets were cut into square supports, heated to 1450 °C (1 °C/min), and sintered for 3 h. The final YSZ supporting electrolytes had dimensions of 10 mm ×10 mm ×1 mm. They were sequentially cleaned in acetone, ethanol, and deionized water and thoroughly dried before sputtering electrode thin films. Patterned stainless steel shielding masks (FotoFab) were used for sputtering electrodes. Figure 1a shows the single-sided polycrystalline YSZ cell that contains one 200-nm-thick Pt CE and two ceria WEs with 300-nm-thick Au current collectors. Dense thin ceria films were sputtered on top of the Au films with elongated Au pads exposed for lead connections. Two thicknesses (50 and 250 nm) of ceria films were investigated in this study. Beneath each of the Au films, 30-nm-thick alumina films were sputtered to block ionic transport from YSZ to Au.[11] The Au, Al_2O_3, and Pt films were sputtered in an AJA sputtering unit. The ceria films were sputtered in a PVD 75 sputter deposition unit from Kurt J. Lesker Co.

As shown in Figure 1a, there is about 350 μm wide of the ceria thin-film WE has direct contact with the supporting YSZ electrolyte. Oxide ions must flow into and out of the ceria WE across this ceria/YSZ interface. The continuous ceria pad also covers ~3 mm on top of the Au current collector. And about 250 μm of uncovered YSZ separates the closest ceria WE edge and the nearest Pt CE edge. All cells were preannealed at 700 °C before electrochemical and XPS measurements. The structural integrity and film thicknesses were evaluated through XRD and scanning electron microscopy (SEM) analyses. Figure 1c shows the cross-sectional SEM image of the 50-nm-thick ceria electrode. Typical grain sizes of ceria films were approximately 20 nm, and their structure is superimposed over the ~1 μm grains of the underlying YSZ support.

Simultaneous AP-XPS and electrochemical characterization were conducted at operating temperatures between 700 and 750 °C with a total pressure of 0.5 Torr 1:1 H_2/H_2O mixtures.

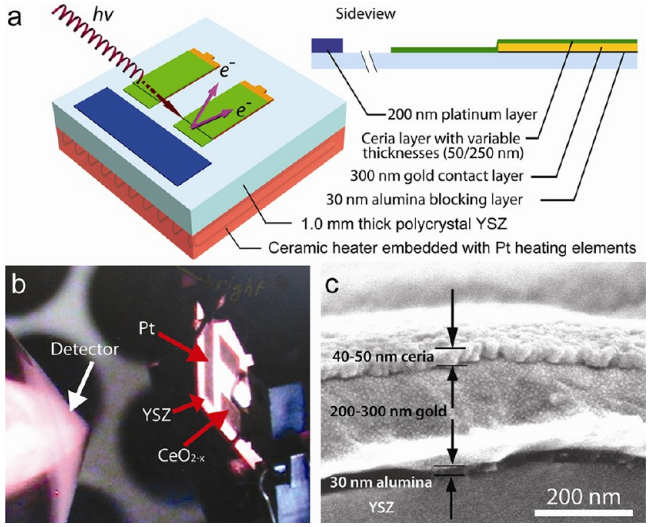

Figure 1. (**a**) Schematic illustration of cell geometry and experimental setup. The single-chamber polycrystalline YSZ cell has one Pt counter electrode (blue) and two ceria working electrodes (green) with Au current collectors (gold). Different thicknesses of ceria films (50 and 250 nm) were sputtered on top of 300 nm thick Au films with elongated Au pads exposed for electrical connections. Underneath the Au films, 30 nm thick alumina films (black) were deposited to block the ionic transport from YSZ to Au. Only one ceria edge has direct contact with the YSZ electrolyte to define current flow region. The outer ceria edge is ~250 μm away from the nearest Pt electrode edge for the 250-nm-thick ceria cell. (**b**) A photograph of an operating cell with the XPS electron detector (the cone) and three electrical contact probes (bent wires). (**c**) Scanning electron micrograph of the cross-section for a fractured 50 nm thick ceria cell.

Single-chamber cells described above were clamped onto a ceramic heater and loaded into the AP-XPS end-stations[15] at beamline 9.3.2 of Advanced Light Source, Lawrence Berkeley National Laboratory. Using a differentially pumped electrostatic lens system, XPS experiments can be performed at background pressures of up to 2 Torr. Spring-loaded probes of the cell mounting platen serve as both clamps and electrical contacts/current collectors for electrodes.[16] In our experiments, H_2 and H_2O were sequentially leaked into the XPS chamber with a partial pressure of ~0.25 Torr each. Once the gas mixture stabilized at the target pressure, the cell was gradually heated to approximately 720 °C over the course of an hour. Actual cell temperatures varied upon the position of cell placed on the heater, and with slight gas pressure variations. Bulk resistance values from impedance data were used to normalize the temperatures to external pyrometer readings. Figure 1b shows the operating cell inside the AP-XPS end-station at ~720 °C.

Two-probe linear sweep voltammetry (LSV) and electrochemical impedance spectroscopy (EIS) measurements were conducted by using a Bio-Logic potentiostat. The WE probe (Au pad) was always grounded to the XPS chamber to facilitate measuring kinetic energy (KE) shifts of photoemitted electrons to assess WE surface potentials.[5,10] The overall cell bias V_{cell} is defined as the potential difference between the Pt CE and the WE Au current collector: $V_{cell} \equiv V_{Pt} - V_{Au}$.

RESULTS AND DISSCUSSION

Electrochemical Measurements. The electrochemical behavior of the cells was initially investigated at ~720 °C with H_2 and H_2O partial pressures of 0.25 Torr each. These

dx.doi.org/10.1021/cs3004243 | ACS Catal. 2012, 2, 2297−2304

conditions give an effective O_2 partial pressure $P_{O2,eff} \approx 9 \times 10^{-24}$ bar. At these temperatures, such low $P_{O2,eff}$ ensures MIEC behavior in the ceria electrode. Figure 2a shows a schematic

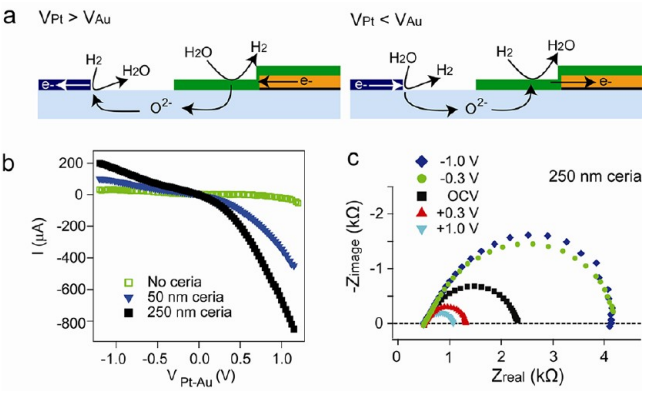

Figure 2. (**a**) Schematic illustrations of cell cross sections illustrating current flow directions and surface reactions under different biases. The following color code identifies the cell components: dark blue, Pt; light blue, YSZ; black, alumina; orange, Au; green, ceria (not drawn to scale). At positive bias, ceria functions as a cathode and promotes electrolysis reactions. At negative bias, the ceria surface promotes hydrogen electro-oxidation as an anode. In both cases, electrons primarily flow laterally along the ceria surface and oxygen ions primarily flow vertically through ceria. (**b**) Linear sweep voltammetry (LSV) polarization curves of cells with different ceria film thicknesses (0, 50, and 250 nm) recorded at ~720 °C with 0.5 Torr 1:1 H_2/H_2O mixtures. (**c**) Electrochemical impedance spectroscopy (EIS) of a 250-nm-thick ceria cell under different applied biases (−1.0, −0.3, OCV, +0.3, and +1.0 V) and the same conditions listed in (**b**).

illustration of reactions on electrode surfaces indicating the need for ceria to have MIEC behavior to exchange electrons with the buried Au current collector and to exchange oxide ions with the YSZ electrolyte support. Figure 2b and 2c show electrochemical characterization: LSV and EIS respectively. Since both the WE and the CE are exposed to the same gas environment, there is no thermodynamic driving force at open circuit voltage (V = OCV when current I = 0.). At open circuit, the electrochemical reactions on both electrodes are in equilibrium with the gas phase, resulting in a near-zero OCV (a few millivolts) that reflects the differences in electrochemical potentials of the two electrodes. Under positive bias ($V_{Pt} > V_{Au}$), water-splitting electrolysis occurs on ceria electrodes (Reaction 1) and hydrogen electro-oxidation (Reaction 2) occurs on Pt electrodes (Figure 2a). Under negative bias ($V_{Pt} < V_{Au}$), the roles of the electrodes are reversed such that water electrolysis occurs on Pt and hydrogen electro-oxidation occurs on ceria.

$$H_2O + 2e^- \rightarrow O^{2-} + H_2 \quad (1)$$

$$H_2 + O^{2-} \rightarrow H_2O + 2e^- \quad (2)$$

The cell electrode geometry requires a lateral movement of electrons and a net vertical transport of oxide ions in ceria thin-film electrodes because of the lack of both an ionic source/drain at Au and an electronic source/drain at YSZ, respectively (Figure 2a). To verify oxide-ion transport pathways, a control cell was fabricated without a ceria film. In this cell, there is no oxide ion pathway between the anode and the cathode because of the Al_2O_3 blocking layer beneath the Au electrode. When biased in either direction, the control cell shows negligible currents (Figure 2b), which verifies the current-blocking function of the alumina layer and confirms the oxide transport pathway in this cell type.

When H_2O electrolysis occurs on ceria ($V_{Pt} > V_{Au}$), the cell currents are significantly higher than those when ceria promotes H_2 electro-oxidation. In the LSV curves in Figure 2b, the two cells with ceria WE show larger currents at positive biases than negative biases. While some of the increase is due to the higher activity of Pt for H_2 oxidation than H_2O electrolysis,[4,17] measurement of local potentials using the KE shifts in the peaks as discussed below show that overpotentials required on the ceria electrode for a given current magnitude are much higher for H_2 electro-oxidation than for H_2O electrolysis. The higher overpotentials associated with the H_2 oxidation on the ceria surface indicates reduced activity for the H_2 electro-oxidation vs H_2O electrolysis. Lower currents at negative bias may also be associated with the lower electronic conductivity of CeO_{2-x} under these conditions. However, the ceria maintains its MIEC character at negative bias as evidenced by expanded electro-active region beyond the Au current collector (see below). To understand the inferior electro-catalytic properties of ceria for H_2 oxidation requires detailed information about changes in ceria surface properties and indicates the value of the AP-XPS to probe surface states and potentials.

In addition to the different behaviors at positive and negative bias, the results in Figure 2b also show that the thicker ceria films have larger currents for both reaction directions relative to thinner films.

Electrochemical impedance spectroscopy was conducted under different applied biases for each cell (Figure 2c: EIS for 250-nm-thick ceria). The electrolyte bulk resistances were obtained from the high frequency intercepts of EIS Nyquist plots. Typically, the electrolyte bulk resistance at 720 °C was within the range of 350−400 Ω. Total polarization resistances under negative bias are significantly larger than those at positive bias, which is also consistent with the LSV data.

Chemical and Potential Mapping of the SOC. To understand the trends observed in the electrochemical behavior of the cells, we performed AP-XPS studies on the single sided SOCs to measure both the binding energies (BE) of the surface species and the shifts in the kinetic energies (KE) of the ejected photoelectrons in operando (~720 °C, 0.25 Torr H_2, 0.25 Torr H_2O, ± 1.2 V). With an applied bias, the Fermi level in the sample material shifts with the local surface potential (V_L), resulting in a kinetic energy shift (ΔKE) of the emitted photoelectrons relative to the unbiased sample.[18] The magnitude of the kinetic energy shift equals the local surface potential according to the relation $\Delta KE = e \cdot V_L$. By measuring ΔKE of photoelectrons of selected elements at various positions in the cell, we can directly assess the local surface potential (V_L) at that position represented by apparent shifts in binding energies (equal to $-\Delta KE$) of the respective elements.[18−21]

At ALS beamline 9.3.2 using AP-XPS end-station, we investigate the trends of potential and oxidation state changes that occur with applied electrochemical bias. Depositing the ceria WE and Pt CE on the same side of the YSZ electrolyte support facilitates full optical access of all component surfaces for the XPS studies. As shown in Figure 3, the new end-station provides XPS spectra as a function of position with a spatial resolution up to 20 μm. Figure 3 shows the C 1s, Si 2p, Ce 4d, and Zr 3d XPS spectra for a 600-μm-long linear window on a

dx.doi.org/10.1021/cs3004243 | ACS Catal. 2012, 2, 2297−2304

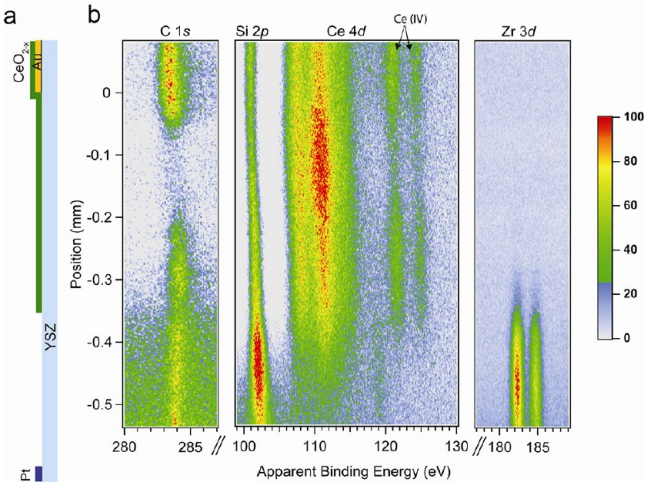

Figure 3. Spatially resolved XPS spectra of the C 1s, Si 2p, Ce 4d, and Zr 3d spectra obtained with a two-dimensional (2-D) area detector on a 250-nm-thick ceria cell at +1.2 V applied potential (~720 °C with 0.5 Torr 1:1 H_2/H_2O mixtures) recorded with 490 eV photon energy. The peaks labeled "Ce^{4+}" are associated only with Ce^{4+} species. The peak intensity is indicated with a color annotation of the intensity percentage on the right. The sideview of schematic cell drawing (**a**) shows the correlation of the cell with the XPS spectra in (**b**).

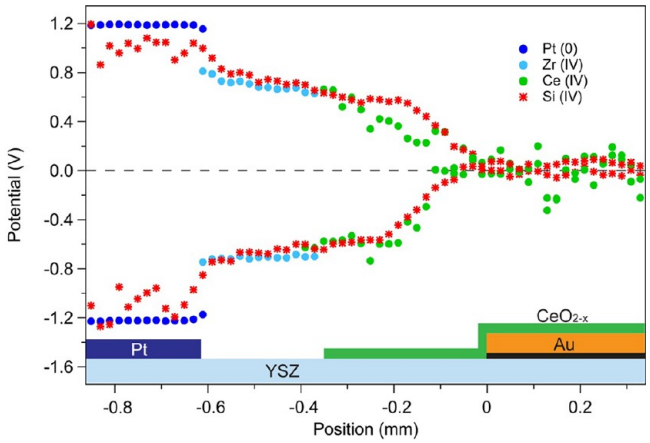

Figure 4. Plots of the local potentials (V_L) calculated from the shifts in photoelectron kinetic energies away from OCV condition. The data shown were collected at +1.2 V (−600 μA) and −1.2 V (+130 μA) applied bias (~720 °C with 0.5 Torr 1:1 H_2/H_2O mixtures). The V_L values of Pt^0, Zr^{4+}, and Ce^{4+} are represented by dark blue, light blue, and green dots, respectively. The red dots show the V_L values of Si^{4+} across the entire cell. The data were extracted from two windows of the XPS area detector that covered the entire cell surface: −0.85 to −0.25 mm for window 1 and −0.25 to +0.35 mm for window 2. The data in window 2 at negative bias were corrected by 0.12 V for beam drift by aligning the Si local potential values at the edges of the two windows.

250-nm-thick ceria electrode. The data in Figure 3 were collected with incident photon energy of 490 eV at +1.2 V cell potential, which promotes water electrolysis on the ceria electrocatalyst. The peak intensity is indicated by the color scale annotation on the right in Figure 3.

Figure 3 shows spatially resolved XPS spectra for different materials of the cell which reveals the electrode edges. The XPS spectrum images are aligned with the cell schematic. At the ceria electrode edge, the Ce 4d peaks start to fade as the Zr 3d peaks start to appear. The lack of sharp edges at interfaces is likely due to material tailing associated with the deposition techniques. Since the Au current collector is covered by the ceria electrode, there is no Au signal in the XPS. As a result, the gold edge was determined by careful calibration of the distance between the Au and Pt pads in the cell photo.

By horizontally slicing the one-dimensional (1-D) XPS maps in Figure 3, the XPS spectra of given elements at given positions can be plotted and fitted. Mapping V_L across the cell can be accomplished by calculating the ΔKE of XPS peak positions of the different elements at different positions. We plot the V_L across from WE to CE in Figure 4. Alternatively, monitoring the V_L values of inert foreign elements that are present in trace amounts, such as silicon, provides a convenient, continuous probe of local surface potential (Figure 4). In addition, analysis of volatile elements such as carbon can reveal regions of electrocatalytic activity. These impurities may come from thin film sputtering, annealing, or sample transfer processes. At high temperature and low gas pressure, these trace elements tend to migrate to the sample surface under certain conditions and are easily detected in the XPS.

The local potentials in the active region extracted from the Si 2p data are virtually identical to the potential maps obtained from the spliced Ce and Zr data shown in Figure 4 and the Ce 4d spectra we reported previously.[5] However, the ΔKE of the Si 2p photoionizations probe the entire surface potential, from CE to WE, without uncertainties associated with changes in materials at interfaces.

Figure 5a shows a narrow region of the potential map calculated from the ΔKE in Si 2p spectra for both the 50 and 250 nm ceria cells from the ceria/YSZ edge to ~200 μm on top of the Au current collector. The ΔKE of Si 2p spectra reveal the local surface potentials and delineate the electrochemically active regions. These active regions are associated with large potential drops on the ceria surface[5] and large shifts in Ce^{3+}/Ce^{4+} concentrations (Figure 5b) that occur close to the Au edge.

Surfaces of $La_{0.8}Sr_{0.2}CoO_{3-\delta}$ (LSC) films were reported to be nearly free of carbonaceous species by elevating the temperature to 220 °C at $P_{O2} = 1 \times 10^{-3}$ bar[22] because of the thermal catalytic oxidation of carbonaceous species, described elsewhere as a "self-cleaning" effect.[23] In contrast, adventitious carbon deposits remain on our noncycled cell surfaces and serve as an excellent marker of electrochemical activity because the carbon removal only happens in the active regions. The C 1s spectra in Figure 3b show the spatially resolved carbon coverage over the sample surface. Figure 5c shows the C 1s peak intensity (i.e., the relative carbon concentration) as a function of position on both 50-nm and 250-nm-thick ceria electrocatalysts. Carbon initially appears over the entire cell, but electrochemical excitation completely removes surface carbon from the active regions of the ceria surfaces after running the cells at ±1.2 V (Figure 3b). At negative bias, the disappearance of carbon in the active region is due to the half-cell reactions of carbon electro-oxidation $C + x{\cdot}O^{2-} \rightarrow CO_x + 2x{\cdot}e^-$ (where $x = 1$ for CO and $x = 2$ for CO_2) on the electrocatalytic ceria surface. At positive bias, surface carbon oxidation in the electrochemically active region may also be facilitated by catalyzed reactions with the high-temperature steam such as the water-gas shift reaction $C + H_2O \rightarrow CO + H_2$.[24−26] Further studies are necessary to quantify more precisely the mechanism of carbon oxidation; however, the carbon oxidation happens primarily in the active regions that involve electrocatalytic oxidation, and carbon

dx.doi.org/10.1021/cs3004243 | ACS Catal. 2012, 2, 2297−2304

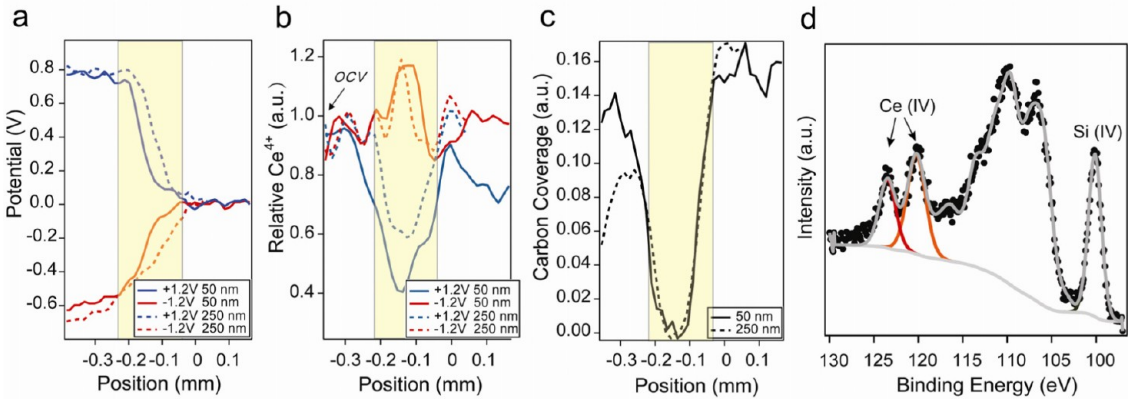

Figure 5. Various signatures of the electrochemically active regions (yellow boxes) on the 50-nm and 250-nm thick ceria electrodes. (**a**) The cell surface potentials calculated from the kinetic energy shifts of Si 2p spectra, showing significant potential drops close to the Au current collectors located at 0 mm. (**b**) The relative concentrations of Ce^{4+} measured in operando at +1.2 V and −1.2 V. The concentrations were determined from the ratio of the high binding energy Ce^{4+} to the total fitted Ce area. The concentration values are normalized to the equilibrium OCV value, which is defined as 1.0. (**c**) The relative carbon concentration on the cell surface, showing absence of carbon in the active regions. (**d**) A cross sectional slice of Ce 4d spectrum (black dots) with two components associated only with Ce^{4+} and a Si^{4+} peak (Si 2p) at ∼100 eV.

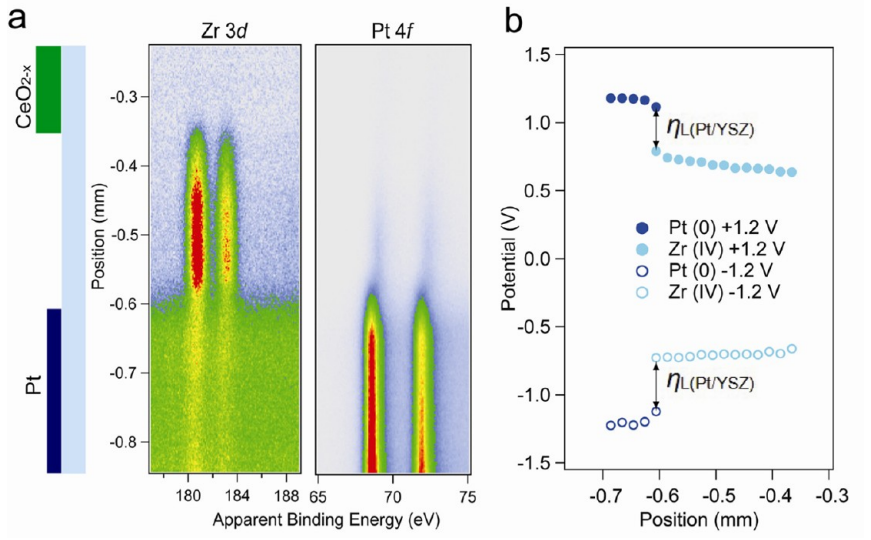

Figure 6. (**a**) Spatially resolved Pt 4f and Zr 3d spectra of the 250-nm-thick ceria cell recorded at −1.2 V applied potential (∼720 °C with 0.5 Torr 1:1 H_2/H_2O mixtures). A schematic drawing of the cell is given at the left. (**b**) The Pt^0 and Zr^{4+} surface potentials across the Pt/YSZ interface. The data were calculated from the kinetic energy shifts of Pt 4f and Zr 3d spectra under +1.2 V and −1.2 V applied biases. The corresponding currents were −618 μA and +148 μA, respectively. The Pt in the contiguous Pt electrode (≤−0.60 mm) has local potentials equal to the applied bias. The interfacial potential difference between Pt and YSZ ($\Delta V_{L(Pt/YSZ)}$), which is equal to the local Pt-YSZ charge transfer overpotential, η_L.

depletion serves as an excellent spatial indicator of electrocatalysis. Oxide transport without electrocatalytic activity in the inactive regions does not affect a change in carbon coverage. Since the carbon oxidation reaction is irreversible, there is a slightly larger area of carbon depletion (Figure 5c) relative to the regions of large surface potential drops (Figure 5a) and cerium oxidation state changes (Figure 5b). As such, the surface carbon that is present on virtually the entire cell can be used as an additional signature of surface electrochemical activity because of its irreversible oxidation reaction. The use of carbon markers of electrocatalytic activity are potentially very useful for optical probes that can easily detect carbon buildup/depletion in functional solid oxide fuel cells.[8]

Overpotential Measurements at the Pt-YSZ Interface. The use of shielding masks during the sputtering of thin film electrodes creates a porous region of Pt at the edge of the Pt-YSZ interface. As a result, the Pt electrode changes from a dense nonporous film to a porous film and eventually to islands of Pt particles on YSZ as one traverse across the Pt-YSZ interface (Figure 6a). The local potential of the contiguous Pt film remains constant and is equal to the applied cell bias. However, the local potentials of the isolated Pt particles on the YSZ electrolyte are shifted relative to the Pt electrode and are equivalent to the YSZ potentials at the same location; that is, they are floating on the YSZ. The porous nature of the edge of the Pt pad at the Pt/YSZ interface provides access to local potentials of Pt and YSZ at the same location. The ability to measure local surface potentials of two different materials at the same location provides a direct measure of the local charge transfer overpotential, V_L. With the single-sided SOCs used in this study, the open circuit voltage is 0 V and therefore the overpotentials are described as the difference in local potentials of any two materials at the same location:

dx.doi.org/10.1021/cs3004243 | ACS Catal. 2012, 2, 2297−2304

$$\eta_L = V_{L2} - V_{L1}$$

The Pt-YSZ local overpotentials (η_L), represented as the difference in Pt and Zr local potential ($\Delta V_{L(Pt/YSZ)}$), are shown in Figure 6b. At the edge of contiguous Pt film and the YSZ electrolyte interface (position −0.62 mm, Figure 6b), the η_L reaches a maximum regardless of the cell bias. Under +1.2 V applied bias, the maximum η_L = 0.4 V at I = −618 μA, whereas at −1.2 V applied bias, a slightly larger η_L = −0.5 V at a much lower current magnitude I = +148 μA. The substantially larger ratio of $\eta_{L(Pt/YSZ)}$ to I at negative bias reflects the higher charge transfer resistance associated with water electrolysis at the Pt/YSZ interface.

By isolating the individual overpotentials and measuring bulk IR losses through electrochemical measurements, we obtain a complete picture of voltage drops across the entire SOC. As illustrated above, the charge transfer overpotentials on Pt (and ceria) are very condition dependent and provide significant insight into the electrochemical processes.

Manipulating CeO_{2-x} Surface Vacancy Density through Electrochemical Excitation. In addition to mapping surface potentials of various elements across the SOC, we have also developed a new Ce 4d fitting protocol and correlate these data with surface CeO_{2-x} vacancies. The Ce 3d photoionizations have been well studied in literature and have well-established fitting profiles for quantitative oxidation state assignments. Previous studies that quantify the ceria oxidation state using XPS focused on single crystal ceria surfaces under well controlled conditions using Ce 3d, O 1s, and/or valence band spectra.[27] In this study, the Ce 4d states are used because of the limitation of the photon energy range at beamline 9.3.2. To expedite data collection and enable Ce oxidation state analysis from 4d photoionizations, we developed a procedure for evaluating Ce 4d spectra. The two Ce 4d peaks at higher binding energies (>118 eV) can be assigned to the spin−orbit doublets associated with Ce^{4+} with the $Ce4d^9O2p^6Ce4f^0$ final state (Figure 5d). The peaks at lower binding energies (<118 eV) in the Ce 4d spectrum are related to mixed valence states of Ce^{3+} and Ce^{4+}. The final states of Ce^{4+} in this region (102−118 eV) correspond to a mixture of $Ce4d^9O2p^5Ce4f^1$ and $Ce4d^9O2p^4Ce4f^2$. The final states of Ce^{3+} in this region (102−118 eV) are associated with a mixture of $Ce4d^9O2p^6Ce4f^1$ and $Ce4d^9O2p^5Ce4f^2$. Therefore, the existence of the spin−orbit doublets at higher binding energies indicates the presence of Ce^{4+}. These data can also be used to extract the Ce^{3+}/Ce^{4+} ratios, as described in the Supporting Information.

In Figure 7, we show both spectral images of the Ce 4d core level region (left) and valence band region (right) of the ceria electrode of a 250 nm SOC. These data were collected at −1.2 V in contrast to the +1.2 V shown in Figure 3. Instead of increasing the Ce^{3+} concentration in the active region, applying a −1.2 V potential decreases the Ce^{3+} surface concentration relative to OCV as shown by the higher intensity of Ce^{4+} peaks in the active region (Figure 7). By adjusting the bias voltage and gas environments of the SOC, we can oxidize or reduce the CeO_{2-x} in the active region (nonequilibrium) relative to that of the nonactive region (equilibrium). The local Ce 4f concentration (BE at 2 eV) is related to the local oxygen vacancy density,[28−30] and therefore serves as an indirect probe of surface vacancy concentrations. As shown in Figure 7, the intensity of the Ce 4f valence state decreases as the cerium in active region as the Ce^{4+} concentration increases (i.e., the ceria becomes more oxidized). We have shown that the surface ceria

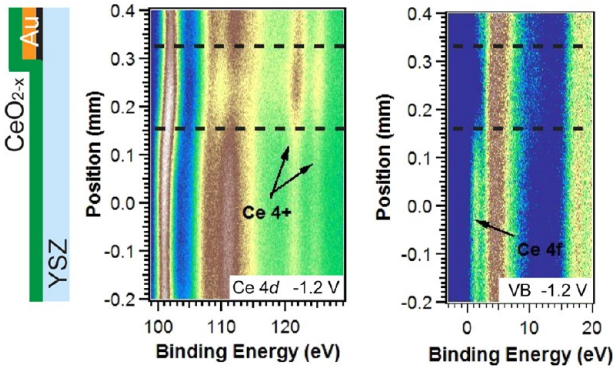

Figure 7. Representative spectral images of Ce 4d and valence band obtained from an 600 μm region extending from the ceria/YSZ edge to ∼100 μm over the Au current collector under −1.2 V. The measurements were taken in 2 mTorr H_2 and 2 mTorr H_2O environment. As shown with the aligned schematic drawing, the top is the ceria layer and is over the gold current collector. The dotted lines denote the electrochemically active regions corresponding to the schematic cell drawing on the left side. The ceria is 250 nm thick on the working electrode. The peaks labeled as Ce^{4+} are associated only with Ce^{4+} specie, its intensity in the active region are higher than that of the nonactive region indicating the ceria in the active region is oxidized under negative applied potential. Spectra were normalized so that each row of pixels has the same integrated intensity to demonstrate the chemical state change of Ce. A decrease of intensity of Ce 4f states in valence band is observed in the active region indicating the decrease of surface oxygen vacancy.

4f concentration and oxygen vacancy concentrations can be electrochemically manipulated; both of which are known to influence the catalytic property of ceria of a given chemical reaction.

To demonstrate the level of control that we can achieve with this method, a "control curve" is shown in Figure 8. The plot shows the correlation between the Ce 4f filling (Y axis) and

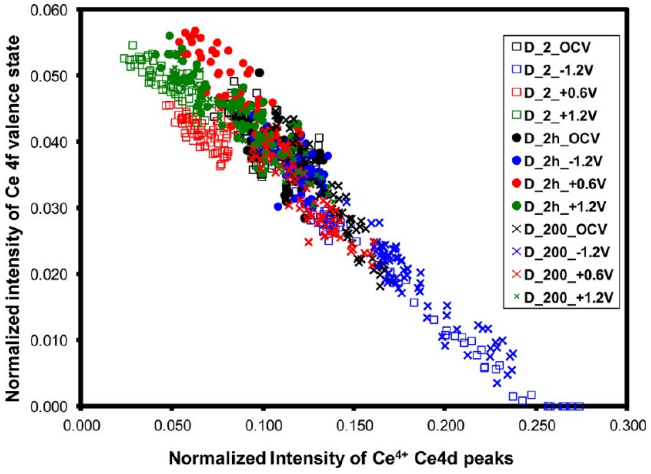

Figure 8. Correlation plot of normalized Ce^{4+} Ce4d peak intensity (coefficient "B" as described in Supporting Information) and Ce 4f valence state normalized peak intensity(coefficient "A" as described in Supporting Information). It consists of data from 3 different gas environments (D_2: 2 mTorr H_2 and 2 mTorr H_2O, D_2h: 2 mTorr H_2 and 200 mTorr H_2O, D_200: 200 mTorr H_2 and 200 mTorr H_2O) and 4 different voltages at each gas environment. This extensive data set would not be possible without the ability to perform in situ electrochemistry or without imaging capability of the endstation.

dx.doi.org/10.1021/cs3004243 | ACS Catal. 2012, 2, 2297−2304

intensity of Ce^{4+} peaks from Ce 4d core level (X axis). It consists of data from 4 different gas environments (symbol shape coded) and 4 different voltages (color coded) at each gas environment. At each operating condition, we obtained XPS spectra at different points across the ceria film for both the Ce 4d and valence band region by taking slices of the spectral images, such as those in Figure 7. As previously discussed, we can fit different Ce 4d peaks and Ce 4f peaks. We plotted the normalized intensity of Ce^{4+} peaks of Ce 4d core level and the normalized intensity of Ce 4f valence state (see Supporting Information). The figure shows that the linear relation between the Ce 4f filling and Ce^{4+} intensity due to localized nature of Ce 4f (Ce^{3+}) defect states. It also shows the broad range of Ce chemical state change that the current method can achieve for a given gas environment. This correlation further illustrates the ability to modulate the Ce 4f concentrations and surface oxygen vacancies through electrochemical modification. Full descriptions of this method will be published elsewhere.

Figure 8 also demonstrates that the imaging capability of APXPS system is an efficient, high throughput characterization tool. The vastly different chemical and electronic states of a compositionally diverse sample, such as our ceria electrode, can be evaluated simultaneously over the 600−800 μm region under identical pressure, temperature, and gas environment. Such capabilities make the APXPS imaging process a high throughput combinatorial approach.

CONCLUSION

The spatially resolved XPS spectra presented here illustrate the operando capabilities of the AP-XPS system for local surface potential mapping and the detection of electrochemically active regions for thin film ceria electrocatalysts. All of the cells with this geometry show similar ranges of electrochemically active regions that extend 150−200 μm away from current collectors on ceria electrodes. The foreign elements (silicon and carbon) present on the SOC electrode serve as trace markers of surface potentials and active regions. The AP-XPS studies on working SOCs provide fundamental information and parameters governing electrochemical reactions of the cells, which could be of significant value to practical cell design and material selection. At the same time, we can use such model SOCs to control the surface oxygen vacancies of the ceria electrode. Such an approach can create different (nonequilibrium) ceria surfaces that are expected to have different catalytic properties both as catalysts and supporting materials. This approach could potentially have significant implications on the fields of SOECs and tunable catalysts.

Impedances and overpotentials in SOCs have historically been analyzed using electrochemical impedance spectroscopy. In this regard, a reference electrode (RE) is normally used to identify electrochemical overpotentials associated with a WE in a "global" sense. This technique is widely used to resolve the overall electrochemical overpotentials for symmetric cell geometries with uniform current flows and equi-potential lines. Careful circuit simulations can be used to determine resistances associated with interfacial charge transfers and related processes. However, the bulk electrochemical impedance technique only detects the overall electrochemical overpotentials and is insensitive to asymmetric variations of activities and charge transport. The AP-XPS methods described here provide local overpotential data and are free of complications associated with reference electrodes. Further studies on this approach are in progress.

ASSOCIATED CONTENT

Supporting Information

Further details on the correlation between the 4f and 4d data from different samples under different conditions are given in Figure S1. This material is available free of charge via the Internet at http://pubs.acs.org.

AUTHOR INFORMATION

Corresponding Author

*E-mail: eichhorn@umd.edu (B.W.E.), gsjackso@umd.edu (G.S.J.), zliu2@lbl.gov (Z.L.).

Author Contributions

⊥Equal contribution.

Funding

This work was funded through the support of the Office of Naval Research through Contract No. N000140510711 (Dr. Michele Anderson program manager). We thank the University of Maryland Nanocenter and the University of Maryland Energy Research Center (UMERC) for support. The Advanced Light Source is supported by the Director, Office of Science, Office of Basic Energy Sciences, of the U.S. Department of Energy under Contract No. DE-AC02-05CH11231.

Notes

The authors declare no competing financial interest.

REFERENCES

(1) Cheng, Z.; Liu, M. *Solid State Ionics* **2007**, *178*, 925−935.
(2) Pomfret, M. B.; Owrutsky, J. C.; Walker, R. A. *Anal. Chem.* **2007**, *79*, 2367−2372.
(3) Pomfret, M. B.; Marda, J.; Jackson, G. S.; Eichhorn, B. W.; Dean, A. M.; Walker, R. A. *J. Phys. Chem. C* **2008**, *112*, 5232−5240.
(4) El Gabaly, F.; Grass, M.; McDaniel, A. H.; Farrow, R. L.; Linne, M. A.; Hussain, Z.; Bluhm, H.; Liu, Z.; McCarty, K. F. *Phys. Chem. Chem. Phys.* **2010**, *12*, 12138−12145.
(5) Zhang, C. J.; Grass, M. E.; McDaniel, A. H.; DeCaluwe, S. C.; El Gabaly, F.; Liu, Z.; McCarty, K. F.; Farrow, R. L.; Linne, M. A.; Hussain, Z.; Jackson, G. S.; Bluhm, H.; Eichhorn, B. W. *Nat. Mater.* **2010**, *9*, 944−949.
(6) Liu, D.-J.; Almer, J. *Appl. Phys. Lett.* **2009**, 94.
(7) Shinoda, K.; Suzuki, S.; Yashiro, K.; Mizusaki, J.; Uruga, T.; Tanida, H.; Toyokawa, H.; Terada, Y.; Takagaki, M. *Surf. Interface Anal.* **2010**, *42*, 1650−1654.
(8) Pomfret, M. B.; Owrutsky, J. C.; Walker, R. A. *Annu. Rev. Anal. Chem.* **2010**, *3*, 151−174.
(9) Salmeron, M.; Schlogl, R. *Surf. Sci. Rep.* **2008**, *63*, 169−199.
(10) DeCaluwe, S. C.; Grass, M. E.; Zhang, C. J.; El Gabaly, F.; Bluhm, H.; Liu, Z.; Jackson, G. S.; McDaniel, A. H.; McCarty, K. F.; Farrow, R. L.; Linne, M. A.; Hussain, Z.; Eichhorn, B. W. *J. Phys. Chem. C* **2010**, *114*, 19853−19861.
(11) Zhang, C.; DeCaluwe, S.; Grass, M.; Liu, Z.; Bluhm, H.; Hussain, Z.; Jackson, G.; Eichhorn, B. *ECS Trans.* **2011**, *33*, 19−24.
(12) Mogensen, M.; Sammes, N. M.; Tompsett, G. A. *Solid State Ionics* **2000**, *129*, 63−94.
(13) Mogensen, M.,Ceria-based electrodes. In *Catalysis by ceria and related materials*; Trovarelli, A., Ed.; Imperial College Press: London, U.K., 2002; pp 453−482.
(14) Ivers-Tiffée, E.; Virkar, A. V. Electrode Polarisations. In *High Temperature and Solid Oxide Fuel Cells*; Subhash, C. S., Keven, K., Eds.; Elsevier Ltd.: Oxford, U.K., 2003; Chapter 9, pp 229−260.
(15) Grass, M. E.; Karlsson, P. G.; Aksoy, F.; Lundqvist, M.; Wannberg, B.; Mun, B. S.; Hussain, Z.; Liu, Z. *Rev. Sci. Instrum.* **2010**, *81*, 053106.
(16) Whaley, J. A.; McDaniel, A. H.; El Gabaly, F.; Farrow, R. L.; Grass, M. E.; Hussain, Z.; Liu, Z.; Linne, M. A.; Bluhm, H.; McCarty, K. F. *Rev. Sci. Instrum.* **2010**, *81*, 086104.

(17) Mizusaki, J.; Tagawa, H.; Miyaki, Y.; Yamauchi, S.; Fueki, K.; Koshiro, I.; Hirano, K. *Solid State Ionics* **1992**, *53*, 126−134.
(18) Ladas, S.; Kennou, S.; Bebelis, S.; Vayenas, C. G. *J. Phys. Chem.* **1993**, *97*, 8845−8848.
(19) Doron-Mor, H.; Hatzor, A.; Vaskevich, A.; van der Boom-Moav, T.; Shanzer, A.; Rubinstein, I.; Cohen, H. *Nature* **2000**, *406*, 382−385.
(20) Siegbahn, H.; Lundholm, M. *J. Electron Spectrosc. Relat. Phenom.* **1982**, *28*, 135−138.
(21) Ertas, G.; Suzer, S. Analysis of surface structures using XPS with external stimuli. In *Surface Chemistry in Biomedical and Environmental Science*; Blitz, J. P., Gun'ko, V. M., Eds.; Springer: New York, 2006; pp 45−58.
(22) Crumlin, E. J.; Mutoro, E.; Liu, Z.; Grass, M. E.; Biegalski, M. D.; Lee, Y.-L.; Morgan, D.; Christen, H. M.; Bluhm, H.; Shao-Horn, Y. *Energy Environ. Sci.* **2012**, *5*, 6081−6088.
(23) Joo, J.-H.; Merkle, R.; Maier, J.; M., K.; Januschewsky, J.; J., F.; A., O.; Hlavathy, Z.; M., H.; Knop-Gericke, A.; Schlögl, R. *Diffusion-Fundamentals.org* **2010**, 12.
(24) Jang, S.-E.; Kim, H. *J. Am. Chem. Soc.* **2010**, *132*, 14700−14701.
(25) Xu, F.; Wang, M.-x.; Liu, Q.; Sun, H.-f.; Simonson, S.; Ogbeifun, N.; Stach, E. A.; Xie, J. *J. Electrochem. Soc.* **2010**, *157*, B1138−B1145.
(26) Ziomek-Moroz, M. E.; Adler, T.; Alman, D. E.; Jablonski, P. D.; Clark, J.; Penner, L. *ECS Trans.* **2008**, *12*, 273−281.
(27) Henderson, M. A.; Perkins, C. L.; Engelhard, M. H.; Thevuthasan, S.; Peden, C. H. F. *Surf. Sci.* **2003**, *526*, 1−18.
(28) Esch, F.; Fabris, S.; Zhou, L.; Montini, T.; Africh, C.; Fornasiero, P.; Comelli, G.; Rosei, R. *Science* **2005**, *309*, 752−755.
(29) Chueh, W. C.; Hao, Y.; Jung, W.; Haile, S. M. *Nat. Mater.* **2012**, *11*, 155−161.
(30) Mullins, D. R.; Overbury, S. H.; Huntley, D. R. *Surf. Sci.* **1998**, *409*, 307−319.

NOTE ADDED AFTER ASAP PUBLICATION

After this paper was published online September 28, 2012, a correction was made to the second paragraph of the Experimental Section. The corrected version was reposted October 5, 2012. Corrections were then made to references 15−17, and the corrected version was reposted October 8, 2012.